

Search for single top quarks in the tau+jets channel using 4.8 fb⁻¹ of pp collision data

V.M. Abazov³⁷, B. Abbott⁷⁵, M. Abolins⁶⁵, B.S. Acharya³⁰, M. Adams⁵¹, T. Adams⁴⁹, E. Aguilo⁶, M. Ahsan⁵⁹, G.D. Alexeev³⁷, G. Alkhazov⁴¹, A. Alton^{64,a}, G. Alverson⁶³, G.A. Alves², L.S. Ancu³⁶, M. Aoki⁵⁰, Y. Arnaud¹⁴, M. Arov⁶⁰, A. Askew⁴⁹, B. Åsman⁴², O. Atramentov^{49,b}, C. Avila⁸, J. BackusMayes⁸², F. Badaud¹³, L. Bagby⁵⁰, B. Baldin⁵⁰, D.V. Bandurin⁵⁹, S. Banerjee³⁰, E. Barberis⁶³, A.-F. Barfuss¹⁵, P. Baringer⁵⁸, J. Barreto², J.F. Bartlett⁵⁰, U. Bassler¹⁸, D. Bauer⁴⁴, S. Beale⁶, A. Bean⁵⁸, M. Begalli³, M. Begel⁷³, C. Belanger-Champagne⁴², L. Bellantoni⁵⁰, J.A. Benitez⁶⁵, S.B. Beri²⁸, G. Bernardi¹⁷, R. Bernhard²³, I. Bertram⁴³, M. Besançon¹⁸, R. Beuselinck⁴⁴, V.A. Bezzubov⁴⁰, P.C. Bhat⁵⁰, V. Bhatnagar²⁸, G. Blazey⁵², S. Blessing⁴⁹, K. Bloom⁶⁷, A. Boehnlein⁵⁰, D. Boline⁶², T.A. Bolton⁵⁹, E.E. Boos³⁹, G. Borissov⁴³, T. Bose⁶², A. Brandt⁷⁸, R. Brock⁶⁵, G. Brooijmans⁷⁰, A. Bross⁵⁰, D. Brown¹⁹, X.B. Bu⁷, D. Buchholz⁵³, M. Buehler⁸¹, V. Buescher²⁵, V. Bunichev³⁹, S. Burdin^{43,c}, T.H. Burnett⁸², C.P. Buszello⁴⁴, P. Calfayan²⁶, B. Calpas¹⁵, S. Calvet¹⁶, E. Camacho-Pérez³⁴, J. Cammin⁷¹, M.A. Carrasco-Lizarraga³⁴, E. Carrera⁴⁹, W. Carvalho³, B.C.K. Casey⁵⁰, H. Castilla-Valdez³⁴, S. Chakrabarti⁷², D. Chakraborty⁵², K.M. Chan⁵⁵, A. Chandra⁵⁴, E. Cheu⁴⁶, S. Chevalier-Théry¹⁸, D.K. Cho⁶², S.W. Cho³², S. Choi³³, B. Choudhary²⁹, T. Christoudias⁴⁴, S. Cihangir⁵⁰, D. Claes⁶⁷, J. Clutter⁵⁸, M. Cooke⁵⁰, W.E. Cooper⁵⁰, M. Corcoran⁸⁰, F. Couderc¹⁸, M.-C. Cousinou¹⁵, D. Cutts⁷⁷, M. Źwiok³¹, A. Das⁴⁶, G. Davies⁴⁴, K. De⁷⁸, S.J. de Jong³⁶, E. De La Cruz-Burelo³⁴, K. DeVaughan⁶⁷, F. Déliot¹⁸, M. Demarteau⁵⁰, R. Demina⁷¹, D. Denisov⁵⁰, S.P. Denisov⁴⁰, S. Desai⁵⁰, H.T. Diehl⁵⁰, M. Diesburg⁵⁰, A. Dominguez⁶⁷, T. Dorland⁸², A. Dubey²⁹, L.V. Dudko³⁹, L. Duflot¹⁶, D. Duggan⁴⁹, A. Duperrin¹⁵, S. Dutt²⁸, A. Dyshkant⁵², M. Eads⁶⁷, D. Edmunds⁶⁵, J. Ellison⁴⁸, V.D. Elvira⁵⁰, Y. Enari¹⁷, S. Eno⁶¹, H. Evans⁵⁴, A. Evdokimov⁷³, V.N. Evdokimov⁴⁰, G. Facini⁶³, A.V. Ferapontov⁷⁷, T. Ferbel^{61,71}, F. Fiedler²⁵, F. Filthaut³⁶, W. Fisher⁵⁰, H.E. Fisk⁵⁰, M. Fortner⁵², H. Fox⁴³, S. Fuess⁵⁰, T. Gadfort⁷⁰, C.F. Galea³⁶, A. Garcia-Bellido⁷¹, V. Gavrilov³⁸, P. Gay¹³, W. Geist¹⁹, W. Geng^{15,65}, D. Gerbaudo⁶⁸, C.E. Gerber⁵¹, Y. Gershtein^{49,b}, D. Gillberg⁶, G. Ginther^{50,71}, G. Golovanov³⁷, B. Gómez⁸, A. Goussiou⁸², P.D. Grannis⁷², S. Greder¹⁹, H. Greenlee⁵⁰, Z.D. Greenwood⁶⁰, E.M. Gregores⁴, G. Grenier²⁰, Ph. Gris¹³, J.-F. Grivaz¹⁶, A. Grohsjean¹⁸, S. Grünendahl⁵⁰, M.W. Grünewald³¹, F. Guo⁷², J. Guo⁷², G. Gutierrez⁵⁰, P. Gutierrez⁷⁵, A. Haas^{70,d}, P. Haefner²⁶, S. Hagopian⁴⁹, J. Haley⁶³, I. Hall⁶⁵, R.E. Hall⁴⁷, L. Han⁷, K. Harder⁴⁵, A. Harel⁷¹, J.M. Hauptman⁵⁷, J. Hays⁴⁴, T. Hebbeker²¹, D. Hedin⁵², J.G. Hegeman³⁵, A.P. Heinson⁴⁸, U. Heintz⁶², C. Hensel²⁴, I. Heredia-De La Cruz³⁴, K. Herner⁶⁴, G. Hesketh⁶³, M.D. Hildreth⁵⁵, R. Hirosky⁸¹, T. Hoang⁴⁹, J.D. Hobbs⁷², B. Hoeneisen¹², M. Hohlfeld²⁵, S. Hossain⁷⁵, P. Houben³⁵, Y. Hu⁷², Z. Hubacek¹⁰, N. Huske¹⁷, V. Hynek¹⁰, I. Iashvili⁶⁹, R. Illingworth⁵⁰, A.S. Ito⁵⁰, S. Jabeen⁶², M. Jaffré¹⁶, S. Jain⁷⁵, K. Jakobs²³, D. Jamin¹⁵, R. Jesik⁴⁴, K. Johns⁴⁶, C. Johnson⁷⁰, M. Johnson⁵⁰, D. Johnston⁶⁷, A. Jonckheere⁵⁰, P. Jonsson⁴⁴, A. Juste⁵⁰, E. Kajfasz¹⁵, D. Karmanov³⁹, P.A. Kasper⁵⁰, I. Katsanos⁶⁷, V. Kaushik⁷⁸, R. Kehoe⁷⁹, S. Kermiche¹⁵, N. Khalatyan⁵⁰, A. Khanov⁷⁶, A. Kharchilava⁶⁹, Y.N. Kharzheev³⁷, D. Khatidze⁷⁷, M.H. Kirby⁵³, M. Kirsch²¹, J.M. Kohli²⁸, A.V. Kozelov⁴⁰, J. Kraus⁶⁵, A. Kumar⁶⁹, A. Kupco¹¹, T. Kurča²⁰, V.A. Kuzmin³⁹, J. Kvita⁹, F. Lacroix¹³, D. Lam⁵⁵, S. Lammers⁵⁴, G. Landsberg⁷⁷, P. Lebrun²⁰, H.S. Lee³², W.M. Lee⁵⁰, A. Leflat³⁹, J. Lellouch¹⁷, L. Li⁴⁸, Q.Z. Li⁵⁰, S.M. Lietti⁵, J.K. Lim³², D. Lincoln⁵⁰, J. Linnemann⁶⁵, V.V. Lipaev⁴⁰, R. Lipton⁵⁰, Y. Liu⁷, Z. Liu⁶, A. Lobodenko⁴¹, M. Lokajicek¹¹, P. Love⁴³, H.J. Lubatti⁸², R. Luna-Garcia^{34,e}, A.L. Lyon⁵⁰, A.K.A. Maciel², D. Mackin⁸⁰, P. Mättig²⁷, R. Magaña-Villalba³⁴, P.K. Mal⁴⁶, S. Malik⁶⁷, V.L. Malyshev³⁷, Y. Maravin⁵⁹, B. Martin¹⁴, J. Martínez-Ortega³⁴, R. McCarthy⁷², C.L. McGivern⁵⁸, M.M. Meijer³⁶, A. Melnitchouk⁶⁶, L. Mendoza⁸, D. Menezes⁵², P.G. Mercadante⁴, M. Merkin³⁹, A. Meyer²¹, J. Meyer²⁴, N.K. Mondal³⁰, R.W. Moore⁶, T. Moulik⁵⁸, G.S. Muanza¹⁵, M. Mulhearn⁸¹, O. Mundal²², L. Mundim³, E. Nagy¹⁵, M. Naimuddin²⁹, M. Narain⁷⁷, R. Nayyar²⁹, H.A. Neal⁶⁴, J.P. Negret⁸, P. Neustroev⁴¹, H. Nilsen²³, H. Nogima³, S.F. Novaes⁵, T. Nunnemann²⁶, G. Obrant⁴¹, D. Onoprienko⁵⁹, J. Orduna³⁴, N. Osman⁴⁴, J. Osta⁵⁵, R. Otec¹⁰, G.J. Otero y Garzón¹, M. Owen⁴⁵, M. Padilla⁴⁸, P. Padley⁸⁰, M. Pangilinan⁷⁷, N. Parashar⁵⁶, V. Parihar⁶², S.-J. Park²⁴, S.K. Park³², J. Parsons⁷⁰, R. Partridge⁷⁷, N. Parua⁵⁴, A. Patwa⁷³, B. Penning⁵⁰, M. Perfilov³⁹, K. Peters⁴⁵, Y. Peters⁴⁵, P. Pétrouff¹⁶, R. Piegaia¹, J. Piper⁶⁵, M.-A. Pleier⁷³, P.L.M. Podesta-Lerma^{34,f}, V.M. Podstavkov⁵⁰, Y. Pogorelov⁵⁵, M.-E. Pol², P. Polozov³⁸, A.V. Popov⁴⁰, M. Prewitt⁸⁰, S. Protopopescu⁷³, J. Qian⁶⁴, A. Quadt²⁴, B. Quinn⁶⁶, M.S. Rangel¹⁶, K. Ranjan²⁹, P.N. Ratoff⁴³, I. Razumov⁴⁰, P. Renkel⁷⁹, P. Rich⁴⁵, M. Rijssenbeek⁷², I. Ripp-Baudot¹⁹, F. Rizatdinova⁷⁶, S. Robinson⁴⁴, M. Rominsky⁷⁵, C. Royon¹⁸, P. Rubinov⁵⁰, R. Ruchti⁵⁵, G. Safronov³⁸, G. Sajot¹⁴, A. Sánchez-Hernández³⁴, M.P. Sanders²⁶, B. Sanghi⁵⁰, G. Savage⁵⁰,

L. Sawyer⁶⁰, T. Scanlon⁴⁴, D. Schaile²⁶, R.D. Schamberger⁷², Y. Scheglov⁴¹, H. Schellman⁵³, T. Schliephake²⁷, S. Schlobohm⁸², C. Schwanenberger⁴⁵, R. Schwienhorst⁶⁵, J. Sekaric⁵⁸, H. Severini⁷⁵, E. Shabalina²⁴, M. Shamim⁵⁹, V. Shary¹⁸, A.A. Shchukin⁴⁰, R.K. Shivpuri²⁹, V. Simak¹⁰, V. Sirotenko⁵⁰, P. Skubic⁷⁵, P. Slattery⁷¹, D. Smirnov⁵⁵, G.R. Snow⁶⁷, J. Snow⁷⁴, S. Snyder⁷³, S. Söldner-Rembold⁴⁵, L. Sonnenschein²¹, A. Sopczak⁴³, M. Sosebee⁷⁸, K. Soustruznik⁹, B. Spurlock⁷⁸, J. Stark¹⁴, V. Stolin³⁸, D.A. Stoyanova⁴⁰, J. Strandberg⁶⁴, M.A. Strang⁶⁹, E. Strauss⁷², M. Strauss⁷⁵, R. Ströhmer²⁶, D. Strom⁵¹, L. Stutte⁵⁰, S. Sumowidagdo⁴⁹, P. Svoisky³⁶, M. Takahashi⁴⁵, A. Tanasijczuk¹, W. Taylor⁶, B. Tiller²⁶, M. Titov¹⁸, V.V. Tokmenin³⁷, I. Torchiani²³, D. Tsybychev⁷², B. Tuchming¹⁸, C. Tully⁶⁸, P.M. Tuts⁷⁰, R. Unalan⁶⁵, L. Uvarov⁴¹, S. Uvarov⁴¹, S. Uzunyan⁵², P.J. van den Berg³⁵, R. Van Kooten⁵⁴, W.M. van Leeuwen³⁵, N. Varelas⁵¹, E.W. Varnes⁴⁶, I.A. Vasilyev⁴⁰, P. Verdier²⁰, L.S. Vertogradov³⁷, M. Verzocchi⁵⁰, M. Vesterinen⁴⁵, D. Vilanova¹⁸, P. Vint⁴⁴, P. Vokac¹⁰, R. Wagner⁶⁸, H.D. Wahl⁴⁹, M.H.L.S. Wang⁷¹, J. Warchol⁵⁵, G. Watts⁸², M. Wayne⁵⁵, G. Weber²⁵, M. Weber^{50,g}, A. Wenger^{23,h}, M. Wetstein⁶¹, A. White⁷⁸, D. Wicke²⁵, M.R.J. Williams⁴³, G.W. Wilson⁵⁸, S.J. Wimpenny⁴⁸, M. Wobisch⁶⁰, D.R. Wood⁶³, T.R. Wyatt⁴⁵, Y. Xie⁷⁷, C. Xu⁶⁴, S. Yacoub⁵³, R. Yamada⁵⁰, W.-C. Yang⁴⁵, T. Yasuda⁵⁰, Y.A. Yatsunenkov³⁷, Z. Ye⁵⁰, H. Yin⁷, K. Yip⁷³, H.D. Yoo⁷⁷, S.W. Youn⁵⁰, J. Yu⁷⁸, C. Zeitnitz²⁷, S. Zelitch⁸¹, T. Zhao⁸², B. Zhou⁶⁴, J. Zhu⁷², M. Zielinski⁷¹, D. Zieminska⁵⁴, L. Zivkovic⁷⁰, V. Zutshi⁵², and E.G. Zverev³⁹

(The DØ Collaboration)

¹Universidad de Buenos Aires, Buenos Aires, Argentina

²LAFEX, Centro Brasileiro de Pesquisas Físicas, Rio de Janeiro, Brazil

³Universidade do Estado do Rio de Janeiro, Rio de Janeiro, Brazil

⁴Universidade Federal do ABC, Santo André, Brazil

⁵Instituto de Física Teórica, Universidade Estadual Paulista, São Paulo, Brazil

⁶University of Alberta, Edmonton, Alberta, Canada; Simon Fraser University, Burnaby, British Columbia, Canada; York University, Toronto, Ontario, Canada and McGill University, Montreal, Quebec, Canada

⁷University of Science and Technology of China, Hefei, People's Republic of China

⁸Universidad de los Andes, Bogotá, Colombia

⁹Center for Particle Physics, Charles University,

Faculty of Mathematics and Physics, Prague, Czech Republic

¹⁰Czech Technical University in Prague, Prague, Czech Republic

¹¹Center for Particle Physics, Institute of Physics,

Academy of Sciences of the Czech Republic, Prague, Czech Republic

¹²Universidad San Francisco de Quito, Quito, Ecuador

¹³LPC, Université Blaise Pascal, CNRS/IN2P3, Clermont, France

¹⁴LPSC, Université Joseph Fourier Grenoble 1, CNRS/IN2P3,

Institut National Polytechnique de Grenoble, Grenoble, France

¹⁵CPPM, Aix-Marseille Université, CNRS/IN2P3, Marseille, France

¹⁶LAL, Université Paris-Sud, IN2P3/CNRS, Orsay, France

¹⁷LPNHE, IN2P3/CNRS, Universités Paris VI and VII, Paris, France

¹⁸CEA, Irfu, SPP, Saclay, France

¹⁹IPHC, Université de Strasbourg, CNRS/IN2P3, Strasbourg, France

²⁰IPNL, Université Lyon 1, CNRS/IN2P3, Villeurbanne, France and Université de Lyon, Lyon, France

²¹III. Physikalisches Institut A, RWTH Aachen University, Aachen, Germany

²²Physikalisches Institut, Universität Bonn, Bonn, Germany

²³Physikalisches Institut, Universität Freiburg, Freiburg, Germany

²⁴II. Physikalisches Institut, Georg-August-Universität Göttingen, Göttingen, Germany

²⁵Institut für Physik, Universität Mainz, Mainz, Germany

²⁶Ludwig-Maximilians-Universität München, München, Germany

²⁷Fachbereich Physik, University of Wuppertal, Wuppertal, Germany

²⁸Panjab University, Chandigarh, India

²⁹Delhi University, Delhi, India

³⁰Tata Institute of Fundamental Research, Mumbai, India

³¹University College Dublin, Dublin, Ireland

³²Korea Detector Laboratory, Korea University, Seoul, Korea

³³SungKyunKwan University, Suwon, Korea

³⁴CINVESTAV, Mexico City, Mexico

³⁵FOM-Institute NIKHEF and University of Amsterdam/NIKHEF, Amsterdam, The Netherlands

³⁶Radboud University Nijmegen/NIKHEF, Nijmegen, The Netherlands

³⁷Joint Institute for Nuclear Research, Dubna, Russia

³⁸Institute for Theoretical and Experimental Physics, Moscow, Russia

- ³⁹*Moscow State University, Moscow, Russia*
⁴⁰*Institute for High Energy Physics, Protvino, Russia*
⁴¹*Petersburg Nuclear Physics Institute, St. Petersburg, Russia*
⁴²*Stockholm University, Stockholm, Sweden, and Uppsala University, Uppsala, Sweden*
⁴³*Lancaster University, Lancaster, United Kingdom*
⁴⁴*Imperial College London, London SW7 2AZ, United Kingdom*
⁴⁵*The University of Manchester, Manchester M13 9PL, United Kingdom*
⁴⁶*University of Arizona, Tucson, Arizona 85721, USA*
⁴⁷*California State University, Fresno, California 93740, USA*
⁴⁸*University of California, Riverside, California 92521, USA*
⁴⁹*Florida State University, Tallahassee, Florida 32306, USA*
⁵⁰*Fermi National Accelerator Laboratory, Batavia, Illinois 60510, USA*
⁵¹*University of Illinois at Chicago, Chicago, Illinois 60607, USA*
⁵²*Northern Illinois University, DeKalb, Illinois 60115, USA*
⁵³*Northwestern University, Evanston, Illinois 60208, USA*
⁵⁴*Indiana University, Bloomington, Indiana 47405, USA*
⁵⁵*University of Notre Dame, Notre Dame, Indiana 46556, USA*
⁵⁶*Purdue University Calumet, Hammond, Indiana 46323, USA*
⁵⁷*Iowa State University, Ames, Iowa 50011, USA*
⁵⁸*University of Kansas, Lawrence, Kansas 66045, USA*
⁵⁹*Kansas State University, Manhattan, Kansas 66506, USA*
⁶⁰*Louisiana Tech University, Ruston, Louisiana 71272, USA*
⁶¹*University of Maryland, College Park, Maryland 20742, USA*
⁶²*Boston University, Boston, Massachusetts 02215, USA*
⁶³*Northeastern University, Boston, Massachusetts 02115, USA*
⁶⁴*University of Michigan, Ann Arbor, Michigan 48109, USA*
⁶⁵*Michigan State University, East Lansing, Michigan 48824, USA*
⁶⁶*University of Mississippi, University, Mississippi 38677, USA*
⁶⁷*University of Nebraska, Lincoln, Nebraska 68588, USA*
⁶⁸*Princeton University, Princeton, New Jersey 08544, USA*
⁶⁹*State University of New York, Buffalo, New York 14260, USA*
⁷⁰*Columbia University, New York, New York 10027, USA*
⁷¹*University of Rochester, Rochester, New York 14627, USA*
⁷²*State University of New York, Stony Brook, New York 11794, USA*
⁷³*Brookhaven National Laboratory, Upton, New York 11973, USA*
⁷⁴*Langston University, Langston, Oklahoma 73050, USA*
⁷⁵*University of Oklahoma, Norman, Oklahoma 73019, USA*
⁷⁶*Oklahoma State University, Stillwater, Oklahoma 74078, USA*
⁷⁷*Brown University, Providence, Rhode Island 02912, USA*
⁷⁸*University of Texas, Arlington, Texas 76019, USA*
⁷⁹*Southern Methodist University, Dallas, Texas 75275, USA*
⁸⁰*Rice University, Houston, Texas 77005, USA*
⁸¹*University of Virginia, Charlottesville, Virginia 22901, USA and*
⁸²*University of Washington, Seattle, Washington 98195, USA*

We present the first direct search for single top quark production using reconstructed tau leptons in the final state. The search is based on 4.8 fb^{-1} of integrated luminosity collected in $p\bar{p}$ collisions at $\sqrt{s}=1.96 \text{ TeV}$ with the D0 detector at the Fermilab Tevatron Collider. We select events with a final state including an isolated tau lepton, missing transverse energy, two or three jets, one or two of them being identified as b quark jet. We use a multivariate technique to discriminate signal from background. The number of events observed in data in this final state is consistent with the signal plus background expectation. We set in the tau+jets channel an upper limit on the single top quark cross section of 7.3 pb at the 95% C.L. This measurement allows a gain of 4% in expected sensitivity for the observation of single top production when combining it with electron+jets and muon+jets channels already published by the D0 collaboration with 2.3 fb^{-1} of data. We measure a combined cross section of $3.84^{+0.89}_{-0.83} \text{ pb}$, which is the most precise measurement to date.

PACS numbers: 14.65.Ha; 14.60.Fg; 13.85.Rm

INTRODUCTION

At the Fermilab Tevatron Collider, top quarks can be produced either in pairs by the strong interaction or

singly by the electroweak interaction. Single top quark production can be used to directly measure the CKM matrix element $|V_{tb}|$ [1], to determine the top quark par-

tial decay width and lifetime [2], to study top quark polarization and to probe physics beyond the standard model (SM) [3]. The production of a single top quark is accompanied by a b quark in the s -channel mode or by both a b quark and a light quark in the t -channel mode, as illustrated in Fig. 1. Besides the s - and t -

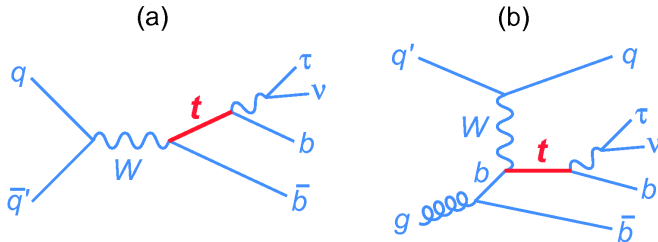


Figure 1: Diagrams for single top quark production in (a) s -channel and (b) t -channel production showing the top quark decays of interest.

channels, single top quarks can also be produced in an associated tW process via $bg \rightarrow tW$. At the Tevatron, this channel has a negligible cross section compared to s - and t -channel production [4]. The s -channel process is referred to as “ tb ” production, where tb includes both $t\bar{b}$ and $\bar{t}b$ states. The t -channel process is abbreviated as “ tqb ”, where this includes $tq\bar{b}$, $t\bar{q}b$, $\bar{t}qb$, and $\bar{t}q\bar{b}$ states. Considering the SM decay modes of the top quark and W boson, single top production and decay results in four channels: electron+jets, muon+jets, tau lepton+jets (tau+jets), and all-jets. Evidence [5–7] and observation [8, 9] of single top quark production in the electron+jets and muon+jets channels and the first direct measurement of $|V_{tb}|$ [5] have been published recently. However, the tau+jets channel has not been measured so far due to the overwhelming jet background at the Tevatron, although signatures involving tau leptons have been explored by D0, for example, in the measurement of the $Z \rightarrow \tau\tau$ cross section [10] and, more recently, in the context of Higgs searches [11]. The measurement of the single top quark cross section in the electron and muon channels is still limited by statistical uncertainties. In this analysis, adding the tau+jets channel increases the signal acceptance by 32% compared to the D0 observation [8]. In addition, the tau+jets channel is a statistically independent channel with different dominant backgrounds and different systematic contributions compared to the electron and muon channels. As such, the tau channel provides an independent measurement of the single top production cross section. In addition, the approach developed in the analysis could be extended to other studies, such as Higgs searches in tau+jets channels, where the cross section to be measured is low and multijet background is dominant.

In this Letter, we report the first direct search for single top quarks in the tau+jets channel. Since the

dominant background source is multijet events, which are poorly modeled by Monte Carlo (MC) simulations, we build most of our background model from an independent sample of multijet data. We then model several smaller background sources using MC and combine them with the multijet sample to complete the background model. We then train a multivariate discriminant to separate the simulated single top signal from the background model. Finally, we extract the single top cross section and combine the result with the existing electron and muon channel measurements.

OBJECT IDENTIFICATION AND EVENT SELECTION

The upgraded D0 detector is described in detail in Ref. [12]. A right-handed coordinate system is used in the analysis. In the system, the z -axis is along the proton direction, ϕ is the azimuthal angle, η is the pseudorapidity, $-\ln[\tan\theta/2]$, where θ is the polar angle, and the true rapidity is defined as, $1/2 \ln[(E + p_z c)/(E - p_z c)]$ [12]. This analysis is based on a sample of D0 Run II data collected between August 2002 and April 2009. Run IIa and Run IIb data are defined as two sub-datasets corresponding to integrated luminosities of 1.0 fb^{-1} and 3.8 fb^{-1} respectively. A new inner layer of silicon microstrip tracking detectors was added to the detector between Run IIa and Run IIb. The additional tracking detectors and the increased instantaneous luminosity in Run IIb change the b -jet identification performance.

The sample considered contains events which have passed one of a list of specialized trigger conditions. The most important ones either set a threshold on the total scalar sum of transverse momenta of the jets in the event, require a minimum transverse momentum of all jets, or select events based on the acoplanarity of the two leading jets sorted in transverse energy. The trigger efficiency in this analysis is $\approx 45\%$.

A hadronically decaying tau lepton appears as a narrow jet in the D0 detector. A tau candidate is a calorimeter cluster reconstructed from all the towers with energy above a threshold within a cone $\mathcal{R} \equiv \sqrt{(\Delta\phi)^2 + (\Delta\eta)^2} < 0.5$ (where ϕ is the azimuthal angle and η is the pseudorapidity) around a seed tower. The tau candidate must have at least one track associated with the cluster, and possibly an additional energetic subcluster of cells in the electromagnetic (EM) section of the calorimeter [10]. Hadronic tau candidates are separated in three types according to the tracking and EM calorimeter information: (1) single track with no EM subclusters, (2) single track with EM subclusters, and (3) two or three associated tracks. The classification is motivated by the decay modes: (1) $\tau^\pm \rightarrow \pi^\pm \nu$ (2) $\tau^\pm \rightarrow \rho^\pm \nu$ and (3) $\tau^\pm \rightarrow \pi^\pm \pi^\pm \pi^\mp (\pi^0) \nu$. We require the tau transverse momentum, p_T^τ , to be larger

than 10, 5, 10 GeV for Type 1, 2 and 3 tau leptons. We also require the transverse momentum of the associated track, p_T^{trk} , to be larger than 7 GeV (5 GeV) for Type 1 (2) tau leptons. For Type 3, the transverse momentum of at least one track, p_T^{trk} , has to be larger than 5 GeV and the sum of the associated track transverse momenta, $\sum_{\text{trk}} p_T^{\text{trk}}$, has to be greater than 7 GeV. Hadronically decaying tau leptons are distinguished from other types of jets using variables such as isolation (defined as $(E_T^{\tau} - E_T^{\text{core}})/E_T^{\text{core}}$ where E_T^{τ} and E_T^{core} are the transverse energy in a cone with radius $\mathcal{R} = 0.5$ and a smaller cone with radius $\mathcal{R} = 0.3$ defined about the same axis), shower width, and shower profiles (a ratio of the E_T 's of the two most energetic calorimeter towers with size $\Delta\phi \times \Delta\eta = 0.1 \times 0.1$ over E_T of the tau candidate). As there is no single tau identification variable which can provide the required background rejection, a multivariate technique is used to combine these features into a single discriminant. Tau identification is then performed by applying kinematic selections as well as a requirement on the multivariate discriminant output.

All other analyses at D0 that use hadronic tau decays except the one reported in this Letter use tau identification relying on a neural network (NN) trained on $Z \rightarrow \tau\tau$ decays and background samples suitable for that signal [10]. In contrast, the multivariate technique used in this analysis for tau identification relies on boosted decision trees (BDT). The BDT technique has been used in previous D0 single top quark analyses [5, 8] and is described in Ref. [6]. In brief, a decision tree is an algorithm which combines selection requirements on a large number of variables with varying discriminating power into a single, more powerful, multivariate discriminant [13, 14]. It can be “boosted” by building the multivariate discriminant through a weighted average score from many decision trees instead of a single tree [15]. A total of 25 well-modeled kinematic variables for each tau type serve as the inputs to BDTs. Table I shows the 10 most discriminative variables with their normalized importance values for tau Types 1, 2 and 3. The importance is derived by an algorithm in which variable usage frequency, separation gains and numbers of events in the splitting nodes are considered [16]. A set of trees is created based on a simulated tau sample from single top quark MC events, and realistic background strongly dominated by fake tau leptons. This fake tau background is extracted from data by requiring events to pass tau jet triggers and applying the kinematic selections given above. Both the signal and background have different kinematics from the standard NN training samples. By changing the technique from neural networks to boosted decision trees we gain $\approx 3\%$, $\approx 8\%$ and $\approx 2\%$ (for Types 1, 2 and 3) signal efficiency for the same background rejection rate (98%). By changing both the technique and the signal and background samples to match the busy single top environment with extra jets we gain $\approx 8\%$, $\approx 20\%$ and $\approx 8\%$ (for Types

1, 2 and 3) signal efficiency yielding $\approx 76\%$, $\approx 69\%$ and $\approx 59\%$ for the same rejection. We require exactly one tau lepton per event.

Jets are reconstructed by an iterative cone algorithm with radius $\mathcal{R} = 0.5$ in rapidity-azimuth space [17]. The highest- p_T jet must have $p_T > 25$ GeV and the second highest- p_T jet $p_T > 20$ GeV while any additional jet must have $p_T > 15$ GeV. The highest- p_T jet must have pseudorapidity $|\eta| < 2.5$ and all other jets $|\eta| < 3.4$. The jets and the tau lepton must be isolated by requiring for their spatial separation in pseudorapidity-azimuth space be larger than 0.5. In order to identify b jets, a neural network is trained on the outputs of three b -jet identification algorithms: secondary vertex, jet lifetime probability, and counting signed impact parameter [18]. All three of these algorithms discriminate b jets from light quark jets by exploiting the signatures of the relatively long lifetime of b hadrons. If the neural network output of a jet is larger than 0.775, the jet is tagged as a b jet. This operating point corresponds in our selected sample to a b -tagging efficiency of 40% and a light-quark tagging rate of 0.4%. We select events with two or three jets, including at least one b jet, in order to enhance the signal-to-background ratio. We also require $20 < \cancel{E}_T < 200$ GeV where \cancel{E}_T is the missing transverse energy which is equal to the negative of the vectorial sum of the transverse energy deposited in the calorimeter by all particles. A tau energy scale correction has been applied and \cancel{E}_T has been corrected for the presence of the tau leptons. We do not exclude electrons that satisfy the tau identification requirement since these electron events provide $>50\%$ of our signal acceptance. However, we veto events with one isolated electron or one isolated muon to make sure the tau+jets sample has no overlap with the electron and muon samples in order to be able to combine the measurements. The data have been split by tau (Types 1 and 2 combined and Type 3), jet multiplicity (two jets and three jets), number of b jets (one b jet and two b jets) and running period, for a total of 16 analysis channels.

We select 3845 b -tagged tau+jets candidate events, among which we expect 72 single top quark events. Table II shows the event yields for all channels combined. About 85% of single top quark events in this sample come from tau Types 1 and 2 and 86% are events with only one b jet. The acceptance times efficiency is 3.0% when considering only hadronic tau leptons.

SIGNAL AND BACKGROUND MODELING

Single top quark events are simulated by the next-to-leading order (NLO) event generator SINGLETOP [19], which is based on COMPEP [20, 21].

Table I: The 10 most discriminative variables with their normalized importance values in the training of the tau identification BDT. The variables listed are explained in Appendix I.

Rank	Tau Type 1	Importance	Tau Type 2	Importance	Tau Type 3	Importance
1	Width $_{\eta,\phi}(\tau)$	2.1×10^{-1}	Width $_{\eta,\phi}(\tau)$	2.8×10^{-1}	Isolation	7.1×10^{-1}
2	Isolation	2.0×10^{-1}	Profile	2.8×10^{-1}	Ratio $_{\tau,\text{trks}}$	3.9×10^{-2}
3	Ratio $_{\tau,\text{trks}}$	9.1×10^{-2}	e_{12}	1.5×10^{-1}	e_{12}	3.0×10^{-2}
4	$E_T^{\text{trk1}}/E_T^\tau$	6.9×10^{-2}	Profile'	5.5×10^{-2}	$E_T^{\text{alltrk-trk1-trk2}}/E_T^\tau$	2.5×10^{-2}
5	Profile'	5.1×10^{-2}	$\delta\alpha$	2.3×10^{-2}	$z_{\text{DCA}}^{\text{trk1}}$	1.9×10^{-2}
6	$E_T^{\text{EMlayer3}}/E_T^\tau$	3.5×10^{-2}	Profile $_{\text{layer3}}$	2.3×10^{-2}	Width $_{\eta,\phi}(\tau)$	1.6×10^{-2}
7	Isolation'	3.2×10^{-2}	Ratio $_{\tau,\text{trks}}$	2.0×10^{-2}	$E_T^{\text{trk1}}/E_T^\tau$	1.5×10^{-2}
8	Profile	3.2×10^{-2}	$E_T^{\text{EMcl2}}/E_T^\tau$	1.7×10^{-2}	Profile $_{\text{layer3}}$	1.3×10^{-2}
9	Ratio $_{\text{EM12},\tau}$	3.0×10^{-2}	$E_T^{\text{trk1}}/E_T^\tau$	1.7×10^{-2}	Width $'_{\eta,\phi}(\tau)$	1.1×10^{-2}
10	Width $'_{\eta,\phi}(\tau)$	2.8×10^{-2}	Isolation	1.5×10^{-2}	$E_T^{\text{EMcls}}/E_T^\tau$	1.1×10^{-2}

Table II: Expected and observed events in 4.8 fb^{-1} of integrated luminosity shown in tau Types 1 and 2, Type 3 channels and all analysis combined. The uncertainties include both statistical and systematic components.

Source	Types 1 and 2	Type 3	Sum
$tb+tb$	61 ± 11	11 ± 2	72 ± 12
$W+\text{jets}$	573 ± 68	107 ± 12	680 ± 104
$Z+\text{jets}$	43 ± 8	17 ± 3	60 ± 10
Dibosons	30 ± 5	7 ± 1	37 ± 6
$t\bar{t}$	170 ± 35	60 ± 12	230 ± 44
Multijets	1444 ± 38	1182 ± 21	2626 ± 98
Total prediction	2321 ± 94	1384 ± 28	3705 ± 153
Data	2372	1473	3845

Since tau leptons are observed as narrow jets of particles in the calorimeter, the main background to single top quark events in the tau+jets channel is multijet production. This is unlike the other leptonic single top channels in which $W+\text{jets}$ events are the main background [8, 9]. We have developed a method to model the multijet background directly from data. The principal steps in this method can be summarized as:

1. Derive a tag rate function (TRF) to describe the probability to b -tag any individual jet in the sample.
2. Apply this TRF to the data sample that has no b -tagged jets.
3. Using simulated events for other physics sources, subtract them from the sample derived in Step 2 to get “pure-multijets”.
4. Normalize the sample derived in Step 3 to data.
5. Combine the derived background sample, pure-multijets, with simulations of other background

sources: $t\bar{t}$, $W+\text{jets}$, $Z+\text{jets}$, dibosons.

In Step 1, we take the ratio of the number of b -tagged jets in our data sample to the total number of jets to define a tag rate: the average probability that a jet is identified as a b jet. We measure the tag rate as a function of jet p_T and η and jet multiplicity.

In Step 2, we apply these TRFs to those events that have no b -tagged jets. This TRFed sample is kinematically similar to our analysis sample, but there is no overlap since we require at least one b -tagged jet in our analysis sample.

In Step 3, we remove physics background sources such as $t\bar{t}$, $W+\text{jets}$, $Z+\text{jets}$ and dibosons. In this procedure, we subtract from the zero-tagged TRFed multijet sample the contaminations of $t\bar{t}$, $W+\text{jets}$, $Z+\text{jets}$ and dibosons. Other background sources are modeled through simulations. These simulations, except the tau decay, have been described in [8]. The program TAUOLA [22] (version 2.5) was used to model the decays of tau leptons including polarization effects. We normalize the $W+\text{jets}$ background to match data by the scale factors that are derived from the study in the electron+jets and muon+jets channels [8]. We apply TRFs to the zero-tagged MC samples to estimate the contamination mentioned above. A similar procedure is used to ensure that any small single top signal contamination in the background data sample is also subtracted.

In Step 4, the multijet events after contamination removal are normalized to data in a multijets-enriched region, as defined by the background-dominated region of the multivariate discriminant described below.

In addition to multijet events modeled by the procedure described above, our background model includes $t\bar{t}$, $W+\text{jets}$, $Z+\text{jets}$ and dibosons modeled directly from simulation. In Step 5, we combine these simulated samples with the data-derived multijet sample.

At the end of the background modeling procedure, we investigate approximately 150 topological variables to

confirm that data and the background model are in good agreement since it is expected that the single top quark events represent only a small fraction, $\approx 2\%$, of the selected data sample. The variables can be categorized in four classes: object kinematics, jet reconstruction, top quark reconstruction and angular correlations. Figure 2 shows four discriminating variables: W boson transverse mass, tau transverse momentum, azimuthal angle between the second-highest- p_T jet and \cancel{E}_T , and cosine of the angle between the tau lepton and a jet candidate that is used to reconstruct the best top quark mass (defined as closest to 170 GeV). These variables are shown for the most sensitive channel: Types 1 and 2, two jets, one of them b tagged.

BOOSTED DECISION TREES

It is expected that single top quark events are only a small fraction of the selected data sample. We use the BDT technique to separate the signal from the background. We also employ the Kolmogorov-Smirnov (KS) test [23] to verify the compatibility of discriminating variables in shape between data and background model. From the ≈ 150 variables studied, 44 to 70 of them are selected as input variables to train BDTs depending on the individual analysis channels. We select only variables which have a KS probability > 0.1 . The KS values of the selected variables are uniformly distributed above this value.

Separate sets of BDTs are built with these variables for each analysis channel. Table III lists the 15 most discriminative variables with their normalized importance values in the most sensitive channel. Figure 3 shows the BDT output with all channels combined, in the region between 0.5 to 1.0, i.e. where the single top quark signal events are expected. Data and the background model are in good agreement in the region. The background-dominated region from 0.0-0.2 is used to define the multijets-enhanced region used in Step 4 of the multijet background modeling procedure.

SYSTEMATIC UNCERTAINTIES

We consider systematic uncertainties from correction factors applied when modeling the signal and background [6]. “Normalization” uncertainty components from the correction factors affect the signal efficiency and the normalization of the background samples, while “shape” uncertainties change the shapes of the distributions for the background and the expected signal. The largest uncertainties arise from W +jets normalization to data, tau identification efficiency, tag rate functions, and jet-flavor correction in W +jets and Z +jets events. Other uncertainties include multijets normalization, integrated

Table III: The 15 most discriminative BDT training variables with their normalized importance values in the most sensitive channel. $\Delta\phi(\text{obj1}, \text{obj2})$ is the azimuthal angle between obj1 and obj2. $\cos\alpha(\text{obj1}, \text{obj2})$ is cosine of the angle between obj1 and obj2. “jet1” and “jet2” are the highest- p_T jet and the second-highest- p_T jet, respectively. “jet1+jet2” is a system consisting of “jet1” and “jet2”. The subscript, “Top-Frame”, indicates that the reference frame is the rest frame of a top quark which is reconstructed using a b -tagged jet, while the subscript “tag” (“untag”) refers to the jet passing (failing) the b -jet identification algorithm. $\sum_{\text{trks in evt}} p_T^{\text{trk}}$ is the transverse momentum of the vectorial sum of all tracks with a cut on the distance of closest approach (DCA) to the primary vertex.

Rank	Variable	Importance
1	W boson transverse mass	5.0×10^{-1}
2	$\Delta\phi(\text{jet2}, \cancel{E}_T)$	3.0×10^{-1}
3	$p_T(\tau)$	3.3×10^{-2}
4	$\cos\alpha(\text{best jet}, \tau)$	2.8×10^{-2}
5	$p_T(\text{jet1}+\text{jet2})$	1.8×10^{-2}
6	$\Delta\phi(\tau, \cancel{E}_T)$	1.5×10^{-2}
7	$\cos\alpha(\text{tag}, \tau)_{\text{TopFrame}}$	1.1×10^{-2}
8	$\Delta\phi(\text{jet1}, \cancel{E}_T)$	1.1×10^{-2}
9	$\sum_{\text{trks in evt}} p_T^{\text{trk}}$	1.0×10^{-2}
10	Best top quark mass	1.0×10^{-2}
11	$p_T(\text{best jet})$	7.6×10^{-3}
12	$Q(\tau) \times \eta(\text{untag})$	5.6×10^{-3}
13	z position of primary vertex	4.9×10^{-3}
14	$\mathcal{R}(\tau, \text{jet2})$	4.6×10^{-3}
15	$\mathcal{R}(\tau, \text{jet1})$	3.9×10^{-3}

luminosity, MC statistics, jet energy scale, jet identification, jet energy resolution, initial- and final-state radiation, jet fragmentation, theoretical cross sections, the reweighting of the jet angular distributions in W +jets events, signal contamination removal, non-multijets contamination, branching fractions, instantaneous luminosity reweighting, parton distribution functions, primary vertex selection, and tau energy scale. The total uncertainty on the background model is 4.2%–19% depending on the analysis channel. Table IV summarizes all sources of uncertainties considered.

Some of the uncertainties are common with the study in the electron and muon channels and have been presented in Ref. [6]. Below are the uncertainties specific to this analysis:

(i) *W+jets normalization to data* (normalization)

The uncertainty is on the scale factors applied to normalize W +jets to match data. Since we use the scale factors derived from the electron+jets and muon+jets study [8], we consider the difference between these two channels as the uncertainty in

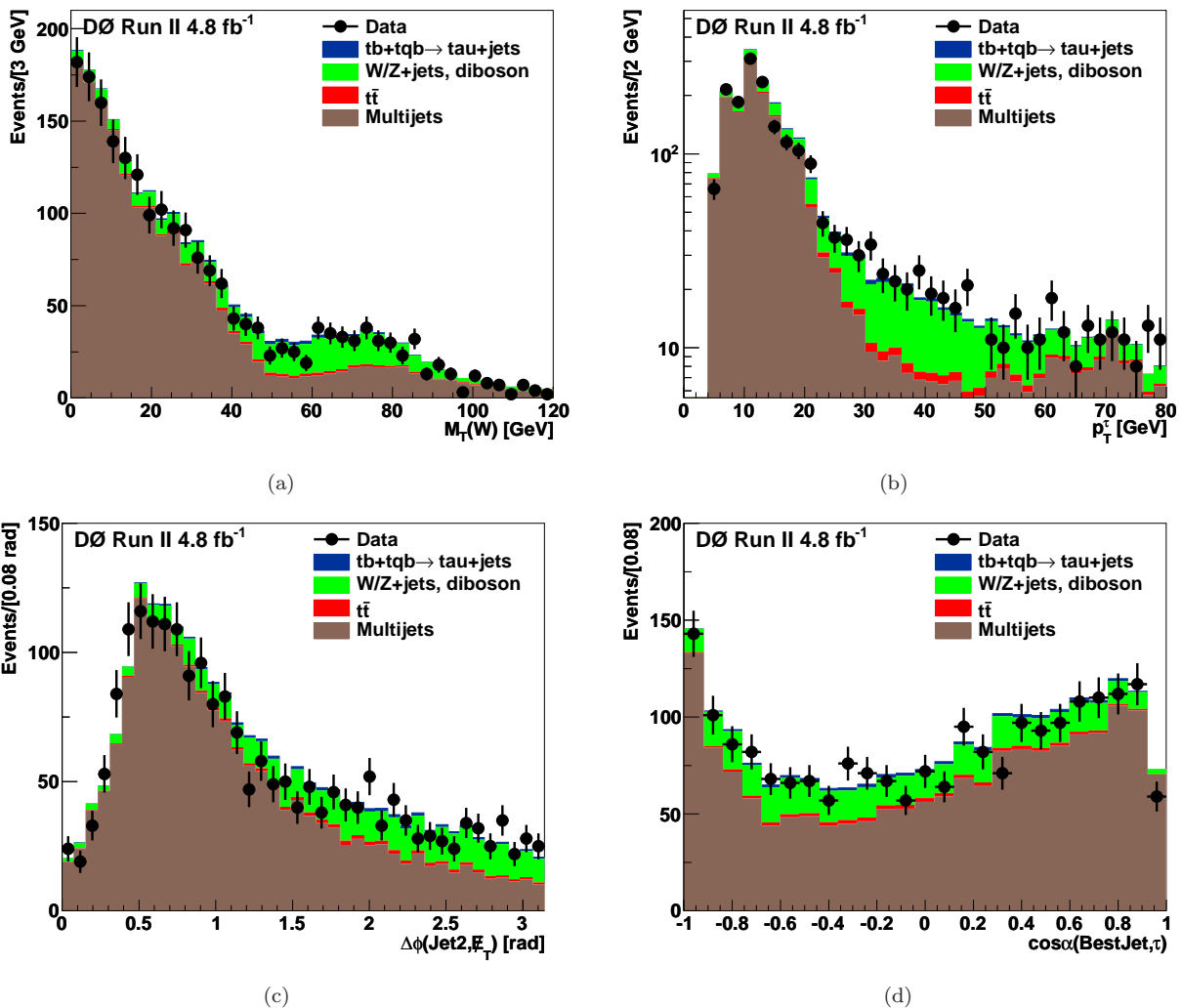


Figure 2: Comparison between data and background distributions in the most sensitive channel: two jets, one b tag, tau Types 1 and 2 combined. (a) W boson transverse mass (b) tau transverse momentum (c) azimuthal angle between the second-highest- p_T jet and \cancel{E}_T , and (d) cosine of the angle between the tau and the best jet candidate that is used to reconstruct the best top quark mass (defined as closest to 170 GeV). In (b), the double-peak structure is caused by different p_T threshold for tau types 1 and 2.

the tau+jets channel.

(ii) *Multijets normalization* (normalization)

The statistical uncertainty of the multijet sample in the BDT region $[0.0, 0.2]$ is used.

(iii) *Tag rate functions* (shape and normalization)

This uncertainty consists of two components: those on the multijet background sample and those on the MC samples related to b -tag modeling. The former is evaluated by raising and lowering the tag rate by one standard deviation of its experimental determination. Uncertainties considered in the latter are from several sources: statistics of the simulated events; the assumed heavy flavor fractions in the simulated multijet sample used for the mistag rate determination; and the choice of parameteriz-

ations [6].

(iv) *Tau identification efficiency* (normalization)

This uncertainty is estimated by the difference in tau identification efficiency between data and MC as derived in a tau-enriched data sample.

(v) *Signal contamination removal* (shape and normalization)

In Step 3 of the background modeling, we reweight single top quark events to remove any small signal contamination. The uncertainty is evaluated by raising and lowering the weighting function by one standard deviation.

(vi) *Non-multijets contamination removal* (shape)

In Step 3 of the background modeling, we subtract

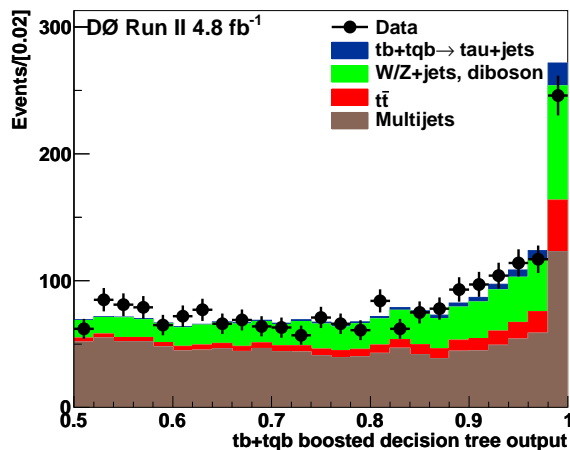


Figure 3: Distribution of BDT output with all channels combined in the signal region ($\text{BDT} > 0.5$). The single top quark signal ($tb + tqb \rightarrow \text{tau} + \text{jets}$) is normalized to the measured cross section.

the non-multijets contamination from the zero-tagged TRFed multijet sample by weighting events. The uncertainty is evaluated by raising and lowering the weighting function by one standard deviation.

(vii) *Tau energy scale* (normalization)

The energy of hadronic tau candidates with low energy is corrected using the energy in the calorimeter and the momentum of the tracks associated to the tau leptons using parameterized single pion response functions. The uncertainty on the scale is estimated by varying these parameterizations.

RESULTS

The number of events observed in data and the shape of the BDT discriminant are consistent with the sum of the signal and background predictions. To estimate the statistical significance of the signal observation we use the same Bayesian approach as in Refs. [5, 6, 8]. This involves forming a binned likelihood as a product over all bins and channels. When measuring a cross section, its central value is defined by the position of the peak in the posterior density, and the 68% interval about the peak is taken as the uncertainty. The posterior density is integrated from 0 until 95% of the posterior area is contained and the upper limit is set at this point. Systematic uncertainties, including all correlations, are reflected in this posterior interval. Assuming a single top quark cross section of 3.46 pb for a top quark mass of 170 GeV [4], we estimate the expected sensitivity to the standard model signal by calculating the ratio of the position of the peak of the expected posterior density to its lower half width.

Table IV: A summary of the relative systematic uncertainties for each of the correction factors or normalizations. The uncertainty shown is the relative error on the correction or the efficiency, before it has been applied to the MC or data samples. We do not show relative systematic uncertainties of the components for shape since they depend on distribution binning.

Relative Systematic Uncertainties	
Components for Normalization	
b -jet fragmentation	2.0%
Branching fractions	1.5%
Diboson cross sections	5.8%
Instantaneous luminosity reweighting	1.0%
Integrated luminosity	6.1%
Initial- and final-state radiation	(0.6–8.0)%
Jet energy resolution	4.0%
Jet energy scale	(4.0–14.0)%
Jet fragmentation	5.0%
Jet identification	1.0%
MC statistics	(0.5–16.0)%
Parton distribution functions (signal acceptances only)	3.0%
Primary vertex selection	1.4%
Multijets normalization	(3.0–14.0)%
Tau energy scale	(1.0–1.5)%
Tau identification efficiency	11.0%
Triggers	5.5%
$t\bar{t}$ cross section	12.7%
W +jets heavy-flavor fraction	13.7%
W +jets normalization to data	(7.0–15.0)%
Z +jets cross section	3.6%
Z +jets heavy-flavor fraction	13.7%
Components for Shape	
ALPGEN reweighting on W +jets sample	—
Non-multijets contamination removal	—
Components for Shape and Normalization	
Signal contamination removal	—
Tag rate functions	—

This yields a ratio of 1.8, i.e. a sensitivity corresponding to approximately 1.8 standard deviation.

In order to test the linearity of our procedure with respect to the single top quark cross section, we generate several ensembles of pseudodatasets by randomly sampling from background model events. We specify five input signal cross sections: 2.0 pb, 3.46 pb, 6.0 pb, 8.0 pb and 10.0 pb and generate ensembles at each value. Each ensemble contains ≈ 2000 pseudodatasets with all systematic uncertainties considered. We then measure the cross

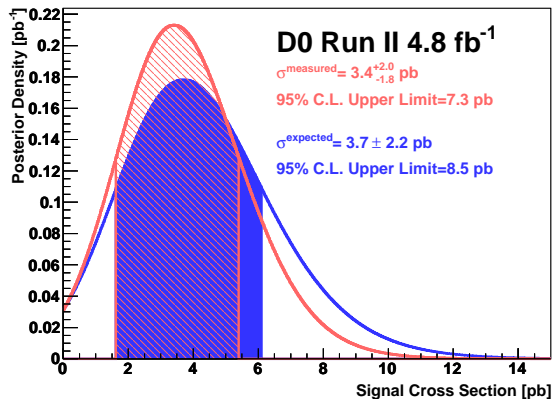


Figure 4: Expected SM and measured Bayesian posterior probability densities for the $tb+tb$ cross section. The shaded regions illustrate \pm one standard deviation from the peak locations.

section in each of the 2000 pseudodatasets at each input value and assess linearity. A linear fit to the measured vs. input cross section gives a slope of 0.99 ± 0.01 and intercept of -0.14 ± 0.05 . Therefore, over the range considered, there is no significant evidence of bias in the measurement procedure.

We obtain an observed posterior density that is used to define an upper limit on the cross section assuming no signal. We can use the same technique to determine an observed cross section and its uncertainty. Assuming no signal, we extract an upper limit of 7.3 pb at 95% C.L. If we perform a cross section measurement, we obtain $3.4^{+2.0}_{-1.8}$ pb. The measured sensitivity, a ratio of the position of the peak of the measured posterior density to its lower half width, is 1.9. Figure 4 shows the expected and measured posterior densities with shaded regions corresponding to \pm one standard deviation from the peak locations.

$t\bar{t}$ CROSS CHECK

As an additional cross check of our background model, we have measured the top quark pair production cross section in the same data sample, including systematic uncertainties and using the same background model and the same techniques as we use to measure the single top quark cross section. We measure a top quark pair production cross section of $10.0^{+2.3}_{-1.6}$ pb, in good agreement with the theoretical expectation, $7.91^{+0.61}_{-0.56}$ pb, from the next-to-next-to-leading-order calculation for a top quark mass of 170 GeV [24], and a recent D0 experimental result, $8.18^{+0.98}_{-0.87}$ pb, also for the same top quark mass [25].

COMBINATION WITH OTHER CHANNELS

As this data sample has no overlap with that used in [8], it is straightforward to combine the results. In the combination, the tau channel and the (electron, muon)+jets channels are treated as two independent channels using the same Bayesian approach used to combine different tau channels above. The ratio of the position of the peak of the expected posterior density to its lower half width is 4.7, compared to 4.5 in the electron+jets and muon+jets channels combined. We gain 4.4% in expected sensitivity by adding the tau+jets channel. The observed posterior density is also calculated and yields a combined cross section of:

$$\sigma(p\bar{p} \rightarrow tb + X, tqb + X) = 3.84^{+0.89}_{-0.83} \text{ pb}$$

Figure 5 shows several recent measurements of single top quark production compared to the theoretical SM prediction [4], 3.46 ± 0.18 pb, calculated for a top quark mass of 170 GeV [4].

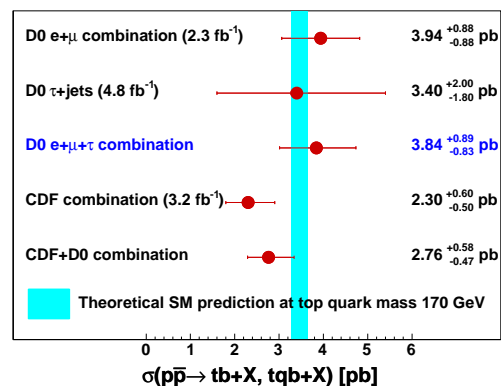


Figure 5: Summary of several recent measurements of single top quark production cross section. The theoretical SM prediction [4] at a top quark mass of 170 GeV is included as a shaded band. The “D0 e+ μ combination” result is taken from [8] while the “CDF combination” result comes from [9] and the “CDF+D0 combination” result from [26].

SUMMARY

In summary, we have presented the first direct study for single top quark production in the tau+jets channel using 4.8 fb^{-1} of integrated luminosity at the D0 experiment. Due to different dominant backgrounds and different systematic uncertainties from the electron and muon channels, the tau+jets channel serves as a channel to independently search for single top quarks. To increase sensitivity, electron+jets events not entering the measurement in the electron+jets channel and where the elec-

tron satisfies tau identification criteria are also included in the tau+jets sample. An upper limit of 7.3 pb at the 95% C.L. for the cross section is obtained. The expected sensitivity of the tau+jets channel alone is 1.8 standard deviations. Adding the tau+jets channel increases the signal acceptance by 32% compared to the D0 observation analysis, which was based on electron+jets and muon+jets channels. The expected sensitivity of the electron+jets, muon+jets and tau+jets combined analysis is 4.7 standard deviations, to be compared to 4.5 standard deviations in electron+jets and muon+jets alone. The measured cross section in all three combined channels is found to be $3.84_{-0.83}^{+0.89}$ pb. This is the most precise measurement to date of the single top quark production cross section.

Acknowledgements

We thank the staffs at Fermilab and collaborating institutions, and acknowledge support from the DOE and NSF (USA); CEA and CNRS/IN2P3 (France); FASI, Rosatom and RFBR (Russia); CNPq, FAPERJ, FAPESP and FUNDUNESP (Brazil); DAE and DST (India); Colciencias (Colombia); CONACyT (Mexico); KRF and KOSEF (Korea); CONICET and UBACyT (Argentina); FOM (The Netherlands); STFC and the Royal Society (United Kingdom); MSMT and GACR (Czech Republic); CRC Program, CFI, NSERC and WestGrid Project (Canada); BMBF and DFG (Germany); SFI (Ireland); The Swedish Research Council (Sweden); and CAS and CNSF (China).

Appendix I: Tau Identification Variable Definitions

$\delta\alpha$: $\sqrt{(\Delta\phi)^2 + (\Delta\eta)^2}$, where $\Delta\phi$ and $\Delta\eta$ are differences between the vector sums of tau tracks and of all EM subclusters [10].

e_{12} : $\sqrt{E_T^{\text{trk}} \cdot E_T^{\text{EMcls}}/E_T^\tau}$, where E_T^{trk} is the sum over all tau-associated tracks' E_T , E_T^{EMcls} is E_T of the sum over EM subclusters. For a system of tau-associated tracks and EM subclusters, the observed tau transverse mass is $e_{12} \times E_T^\tau \times \delta\alpha$ in the small angle approximation [10].

$E_T^{\text{alltrk-trk1-trk2}}$: transverse energy of tracks except the first two highest- p_T tracks.

E_T^{EMcl2} : transverse energy of the second-highest- p_T EM subcluster.

E_T^{EMlayer3} : transverse energy deposited in the 3rd layer of the EM calorimeter within a cone $\mathcal{R} < 0.5$.

E_T^{trk1} : transverse energy of the highest- p_T track.

Isolation: $\frac{\sum p_T^{\text{trk}}}{\sum p_T^{\text{trk}}}$, where $\sum p_T^{\text{trk}}$ is the sum of p_T non-tau-associated tracks within a cone size 0.5 and $\sum p_T^{\text{trk}}$ is the sum over all tau-associated tracks' p_T .

Isolation': if $|\eta_{\text{det}}| \leq 1.0$, where η_{det} is tau's detector pseudorapidity, which is defined with respect to the center of the detector, Isolation' = Isolation. If $|\eta_{\text{det}}| > 1.0$, Isolation' = Isolation/($1.5 \times |\eta_{\text{det}}| - 0.5$).

Profile: $\frac{E_{T1} + E_{T2}}{E_T^\tau}$ where E_{T1} and E_{T2} are the transverse energies of the two highest- p_T calorimeter towers in a tau object.

Profile': if $|\eta_{\text{det}}| \leq 1.5$, Profile'=Profile. If $|\eta_{\text{det}}| > 1.5$, Profile' = Profile $\times (0.67 + 0.22 \times |\eta_{\text{det}}|)$.

Profile_{layer3}: a ratio of E_T of the highest p_T EM subcluster over E_T deposited in the 3rd layer of the EM calorimeter within a cone $R < 0.5$.

Ratio_{EM12, τ} : $\frac{E^{\text{EM1}} + E^{\text{EM2}}}{E^\tau}$ where E^{EM1} and E^{EM2} are energies deposited in the 1st and 2nd layers of the EM calorimeter.

Ratio _{τ ,trks}: $\frac{E_T^\tau}{E_T^\tau + \sum p_T^{\text{trk}}}$

Width _{η,ϕ} (τ): tau shower width, the root sum of squares of the E_T -weighted η - ϕ distance of all calorimeter towers with respect to the tau axis, i.e., $\sqrt{\sum_{i=1}^n (\Delta\eta_i^2 + \Delta\phi_i^2) \frac{E_{Ti}}{E_T}}$ where i is the index of calorimeter towers and $E_T = \sum_i E_{Ti}$.

Width' _{η,ϕ} (τ): Width _{η,ϕ} (τ)/($1.0 + 0.29 \times |\eta_{\text{det}}|$).

$z_{\text{DCA}}^{\text{trk1}}$: z position of the highest- p_T track at DCA.

-
- [1] G.V. Jikia and S.R. Slabospitsky, Phys. Lett. B **295**, 136 (1992).
 - [2] D.O. Carlson, C.-P. Yuan arXiv:hep-ph/9509208
 - [3] T.M.P. Tait, C.-P. Yuan, Phys. Rev. D **63**, 014018 (2000).
 - [4] N. Kidonakis, Phys. Rev. D **74**, 114012 (2006).
 - [5] V.M. Abazov, et al., (D0 Collaboration), Phys. Rev. Lett. **98**, 181802 (2007).
 - [6] V.M. Abazov, et al., (D0 Collaboration), Phys. Rev. D **78**, 012005 (2008).
 - [7] T. Aaltonen, et al., (CDF Collaboration), Phys. Rev. Lett. **101**, 252001 (2008).
 - [8] V.M. Abazov, et al., (D0 Collaboration), Phys. Rev. Lett. **103**, 092001 (2009).
 - [9] T. Aaltonen, et al., (CDF Collaboration), Phys. Rev. Lett. **103**, 092002 (2009).
 - [10] V.M. Abazov, et al., (D0 Collaboration), Phys. Rev. D **71**, 072004 (2005).
 - [11] V. M. Abazov, et al., (D0 Collaboration), Phys. Rev. Lett. **102**, 251801 (2009).

- [12] V. M. Abazov, et al., (D0 Collaboration), Nucl. Instrum. Meth. Phys. Res. A565, 463 (2006).
- [13] L. Breiman, J. Friedman, C. J. Stone, and R. A. Olshen, *Classification and Regression Trees* (Wadsworth, Stamford, 1984).
- [14] D. Bowser-Chao and D. L. Dzialo, Phys. Rev. D **47**, 1900 (1993).
- [15] Y. Freund and R. E. Schapire, in *Machine Learning: Proceedings of the Thirteenth International Conference*, edited by L. Saitta (Morgan Kaufmann, San Francisco, 1996), p. 148.
- [16] A. Hocker et al., *TMVA - Toolkit for Multivariate Data Analysis, Users Guide* (2009); L. Breiman et al., *Classification and Regression Trees*, Wadsworth (1984).
- [17] Jets are defined using the iterative seed-based cone algorithm with radius $\sqrt{(\Delta\phi)^2 + (\Delta y)^2} = 0.5$, including midpoints as described on pp. 47–77 in G. C. Blazey et al., in *Proceedings of the Workshop on QCD and Weak Boson Physics in Run II*, edited by U. Baur, R.K. Ellis, and D. Zeppenfeld (FERMILAB-PUB-00-297, 2000).
- [18] T.P. Scanlon, FERMILAB-THESIS-2006-43.
- [19] E.E. Boos, et al., Phys. Atom. Nucl. 69, 1317 (2006). We use SINGLETOP version 4.2p1.
- [20] E.Boos et al., Nucl. Instrum. Meth. A 534, 250 (2004).
- [21] A.Pukhov et al., INP MSU report 98-41/542.
- [22] S. Jadach, et al., Comput. Phys. Commun. 76, 361 (1993).
- [23] F. James, *Statistical Methods in Experimental Physics* 2nd edition, New Jork: World Scientific (2006).
- [24] N. Kidonakis and R. Vogt, Phys. Rev. D 68, 114014 (2003).
- [25] V. M. Abazov, et al., (D0 Collaboration), Phys. Rev. D 80, 071102(R) (2009).
- [26] Tevatron Electroweak Working Group, for the CDF Collaboration and the D0 Collaboration, arXiv:0908.2171v1 [hep-ex]; FERMILAB-TM-2440-E.